Vector Along-Track Interferometry for Ocean Current Mapping

Ernesto Rodríguez, David Imel and Søren Madsen

Jet Propulsion Laboratory

California Institute of Technology

Pasadena, California 91109

For additional information contact er@dionysus.jpl.nasa.gov

Abstract

We examine the feasibility of measuring Along-Track Interferometric (ATI) vector ocean velocities using the azimuth beamwidth of the SAR antenna to obtain angular diversity, at the expense of spatial resolution. A simple model of the measurement is introduced for point targets and moving ocean surfaces to help interpret the velocity measurements. Due to the shorter integration times used in forming the synthetic aperture, this model is easier to interpret than conventional SAR and interferometric SAR ocean scattering models. We present tradeoff considerations for the processing parameters, and use the JPL L-Band along-track interferometric system as an example. We also present an assessment of the accuracy of the method, showing the feasibility of mapping vector ocean currents with satisfactory accuracy at the scales of interest to oceanographers. Finally, we present an example of vector currents taken in Currituck Sound, North Carolina.

1. Introduction

Along-Track Interferometry (ATI) [1] has shown great promise in measuring the component of ocean motion which lies along the nominal SAR look direction at high range resolution ($\sim$ 10 meters). This resolution is the appropriate scale for measuring wave motion, and promising results for measuring wave spectra using ATI have been reported [2?], [3], [4]. However, many oceanographic applications are concerned with vector velocities at lower spatial resolution. The length scales of interest for large scale oceanography are on the order of the Rossby radius of deformation (~ 30km), while the velocities of interest range between $\mathcal{O}(1\text{m/s})$ for boundary currents, to $\mathcal{O}(10\text{cm/s})$ for eddies and $\mathcal{O}(1\text{cm/s})$ for weak open ocean currents, For coastal applications, or for resolving internal waves, a finer resolution is needed, but a spatial resolution of ()(100 m) is still sufficient for most applications. As a point of comparison, the TOPEX altimeter system for measuring global geostrophic currents has an accuracy $\mathcal{O}(5\text{cm/s})$ on scales of . . . 100km. ATI has also been used successfully to map the radial component of large scale currents [5], coastal currents [1], [6], [7], and internal wave signatures [8]. The limitation of the measurements to radial only

velocities, however, places a severe constraint on the usefulness of such data for oceanographic applications. This limitation can be overcome by flying orthogonal ATI passes over the same site [7], but this severely constrains the spatial coverage that can be practically achieved. The purpose of this paper is to introduce a new technique to measure vector surface currents using a single pass ATI measurement. We will show that the accuracy and resolution of this technique are adequate for many oceanographic applications, making vector ATI a useful new tool for oceanographic investigation.

While the range resolution of ATI can be quite high, the coherence time of the ocean sets fundamental limitations on the azimuth resolution [9), [1(1], [1)], 112], 113]: the effective synthesized antenna length is equal to the product of the platform velocity and the coherence time of the ocean return. The resulting azimuth resolution cell size is approximately given by

$$\delta x \approx \frac{\lambda h}{2 v \tau_c \cos\theta} \tag{1}$$

where λ is the electromagnetic wavelength, h is the platform height, v is the platform velocity, τ_c is the ocean coherence time, and θ is the incidence angle. Observations [14], [15], [16] indicate the ocean coherence time at L-Band varies approximately between (4.05s to 0.25s. For the JPL L-Band SAR system [1 6], whose relevant parameters are presented in Table 1, the corresponding achievable azimuth resolution can vary between 25m and 125m for these correlation times, which is much degraded relative to the intrinsic range resolution.

Using this line of reasoning, there is no advantage for ocean applications in trying to increase the azimuth resolution by using the long integration times appropriate for imaging of stationary targets. In this paper, we propose an alternate use for the data collected while a given ocean patch remains in the radar beam: instead of using one long integration period (of several seconds duration), we propose that many short integration periods (on the order of the field correlation time) be used, together with Doppler sharpening, and the interferometric phase, to interrogate the same surface patch from a variety of azimuth look directions (see Figure 1). The interferometric phase difference, Φ_i, resulting from each of these measurements will be proportional to the projection of the surface velocity vector $\vec{U}$

along the look direction given by the unit vector $\hat{n}_i = \hat{v} \sin\phi_i + \hat{n}_0 \cos\phi_i$:

$$\Phi_i = 2k\tau \hat{n}_i \cdot \vec{U} = 2k\tau (U_\perp \cos\phi_i + U_\parallel \sin\phi_i) \qquad (2)$$

In the previous equation, k is the electromagnetic field wavenumber, τ is the delay time between ATI measurements, and ϕ_i is the azimuth angle in the plane defined by the platform velocity and the broadside direction to the scattering patch. If measurements are made at a sequence of ϕ_i's, both components of the surface velocity can be determined by least squares fitting the phase difference data using all the observation angles. In the next section, we will give a procedure for determining these ϕ_i's using the interferometric phase differences and Doppler sharpening.

The technique proposed here is similar in flavor to one proposed by Madsen [1'7] to measure vector velocities using a split beam antenna. In that technique, two narrow physical beams, displaced by 90° relative to each other and by $\pm 45^\circ$ relative to the flight path, are used to isolate an ocean patch in angular space so that orthogonal components of the surface velocity along the beam directions can be obtained using conventional ATI processing. The technique proposed here has the advantage that one can measure vector velocities using a single beam, so that the current ATI configurations can be used to derive vector velocities without any hardware modification. It has the additional advantage that both components of the surface velocity are determined simultaneously, whereas in the split beam technique each component is determined at different times. The present technique has the disadvantage that range resolution must be sacrificed in order to obtain reasonable velocity accuracies. The spatial resolutions achievable, however, are satisfactory for many oceanographic applications.

The ouline of this paper is as follows. In the first section, we present the algorithm to determine the velocity of a point scatterer. The procedure for determining the vector velocity is the same for an ocean velocity field, but in this simplified case the resultant velocity can be related in an unambiguous fashion to the target velocity. In the next section, we present a simplified model for the return from a moving ocean with the aim of interpreting what the measured velocity represents physically. Due to the short integration

times, the measured quantities are more easily related to physical quantities than in the conventional long integration time processing. In the third section, we study how the integration time and range resolution may be set to optimize system performance. In the fourth section, we discuss random and systematic measurement errors and give formulas for determining system accuracy. Finally, in the last section, we present an example of vector-ATI (VATI) derived velocities for an ocean scene.

2. Vector ATI for Point Targets

As presented in the introduction, the idea behind the VATI algorithm is simple: radial velocities for many azimuth angles are obtained by forming Doppler sharpened interferograms. Since each of the measured radial velocities represents a projection of the true velocity vector along different directions, the true velocity vector can be reconstructed as long as the azimuth incidence angles are known. However, the incidence angles are not known *a* priori: in conventional Doppler sharpening from stationary scenes there is a one-to-one mapping between Doppler shift and azimuth direction. For a moving target, a relationship still exists, but it now depends on the target velocity itself, which is the quantity we are trying to estimate! To overcome this limitation, we use the ATI radial velocity estimate itself to estimate the target's trajectory in range Doppler space, as we show in detail below.

As with conventional SAR processing, it is useful to look at the same technique from a variety of perspectives. In the main body of this paper, we adopt a geometrical perspective which is intuitively appealing. A spectral perspective can also be adopted, and that approach is useful in understanding how a target velocity in the along-track direction, which corresponds to a platform flying with a different velocity than the one used for processing, can be determined by using the return from two offset antennas to estimate the image along-track shift. This approach is similar in flavor to conventional SAR autofocus algorithms [18]. This alternate point of view is presented in Appendix A.

To obtain the Doppler sharpened ATI return from a point target, let us model the

scattered field at, the reference ATI antenna as

$$E(t) = G(t)e^{-2ikr(t)} \tag{3}$$

where t is slow time, $G(t)$ represents the weighting due to the antenna pattern, and the factor $e^{-2ikr(t)}$ represents the two-way propagation phase from the radar to theta-get. The field at the second antenna is given by an identical expression with the exception that the distance to the target, r, is evaluated at $(t+\tau)$, where τ is the time required for the second antenna to revisit the location of the first antenna.

The ith l>o~)plcr--sharpcncd measurement for the first antenna is obtained by Fourier transforming the field over a time interval T centered about slow time t_i

$$E_i^{(1)}(\Omega) = \int_{t_i-T/2}^{t_i+T/2} dt\ W(t-t_i)E(t)e^{-i\Omega t} \tag{4}$$

$$= \int_{t_i-T/2}^{t_i+T/2} dt\ W(t-t_i)G(t)e^{-2ikr(t)}e^{-i\Omega t} \tag{5}$$

where $W(t-t_i)$ is a weighting function (of duration $\sim T$) introduced to reduce azimuth sidelobes. If T is short enough (in a sense which will be made more clear below), one can expand

$$r(t) \approx r(t_i) + \dot{r}(t_i)\ (t-t_i) + \cdots \equiv r_i + \dot{r}_i(t-t_i) + \quad . \tag{6}$$

where $\dot{r}_i$ is the radial component of the the velocity along $\hat{r}_i$, the direction from the synthetic aperture center to the target

$$\dot{r}_i = \hat{r}_i \cdot \left(\vec{U} - \vec{v}\right) \tag{7}$$

where $\vec{v}$ and U are the platform and target velocity vectors, respectively. Since the illumination due to the antenna changes veslowly compared to T, the integral can be evaluated to obtain

$$E_i^{(1)}(\Omega) = G_i e^{-2ikr_i}\tilde{W}(\Omega + 2k\dot{r}_i)e^{-i\Omega t_i} \tag{8}$$

where G_i represents the antenna gain pattern in the synthesized direction, r_i is the range to the target at the center of the synthesized antenna, and $\tilde{W}$, the Fourier transform of W, is the point target response in Doppler space. The effect of target motion on this term is

to shift the location of the peak of the point target response relative to a stationary target try an amount equal to the Doppler shift of the target relative to a stationary observer.

Assuming that the change in range during the revisit time, τ, is much smaller than the range resolution, the return signal at the second ATI antenna is identical with the exception of a phase factor $\exp[-2ik\hat{r}_i \cdot \vec{U}_\tau]$, which represents the phase due to motion of the target in the radial direction between the formation of the two synthetic apertures. The interferometric return can be written as:

$$E_i^{(1)}(\Omega)(E_i^{(2)}(\Omega))^* = |G_i|^2 |\hat{W}(\Omega - 2k\hat{r}_i)|^2 \exp[-2ik\hat{r}_i \cdot \vec{U}_\tau] \quad (9)$$

where we have assumed that the change in Doppler shift from the target to the second antenna is much smaller than the width of the Doppler-space point target response, so that one can approximate both point target responses as being centered on the same Doppler. This approximation is valid as long as $2(v/\lambda)(U_\tau)/\lambda r_i << 1$, which will always be valid for the cases we are considering. As expected, one can obtain an estimate of the velocity in the radial direction using only the phase of the interferometric product. By acquiring a set of these measurements along different directions, one can solve for the full vector velocity.

In order to proceed, it is necessary to formulate an approach which allows for the estimation of the range and the Doppler shift to the resolution cell as a function of time. This is possible because the interferometric phase difference is due to the target motion alone, so that a correction can be applied to the stationary target angle-Doppler relationship by using the measured phase difference to provide the correction term (see Figure 2). once the azimuth angle is known, the range of the target is also known (Figure 1). The following paragraphs present an approximate procedure for accomplishing this mapping.

Select a reference value of the Doppler shift, Ω_0, (e.g., the expected Doppler for a stationary target in the antenna. boresight direction), and perform unfocussed ATI compression as described above to estimate the interferometric phase difference (using range multi-looking, as described below, to obtain a stable estimate) The interferometric phase difference will be given by

$$\Phi_0 = 2k\tau(U_\perp \cos\phi_0 + U_\parallel \sin\phi_0) \quad (10)$$

On the other hand, the Doppler shift can be expressed in terms of the same parameters as

$$\Omega_0 = 2k\left[\left(v - U_{\|}\right)\sin\phi_0 - U_{\perp}\cos\phi_0\right) \tag{1.1}$$

where, in the convention used here, positive target velocity implies that the target is moving away from the radar. From equations (10) and (11), it is possible to solve for $\sin\phi_0$, to obtain

$$\sin\phi_0 = \frac{\Phi_0}{2kv_T} + \frac{\Omega_0}{2kv} \tag{12}$$

From Figure 1, one can also write

$$\sin\phi_0 = \frac{vt_0}{r_0} \tag{13}$$

where r_0 corresponds to the range to the target at time t_0. We have adopted the convention that t = O corresponds to the time for closest approach if we take t_0 to correspond to the time corresponding to the center of the integration interval. From this equation, it is possible to solve for ρ_0, the range at closest approach (see Figure 1):

$$\rho_0 = r_0\cos\phi_0 = r_0\sqrt{1 - \left(\frac{\Phi_0}{2kv_T} + \frac{\Omega_0}{2kv}\right)^2} \tag{14}$$

Given this range at closest approach, it is possible to calculate the range and azimuth angle to the same cell for all subsequent integration intervals

$$r_i = \sqrt{\rho_0^2 + (vt_i)^2} \tag{15}$$

$$\text{sill} \quad \phi_i = \frac{vt_i}{\rho_0} \tag{16}$$

and t_i is the time corresponding to the center of the ith integration time.

While it is now possible to follow the target in range-angle space, it is also required to follow it in range-Doppler space: given an azimuth angle, the corresponding Doppler parameter, used for focusing the return in the direction of the target, can then be determined. The Doppler shift to the target for the ith synthetic aperture is given by

$$\Omega_i = 2k\left[v\left(1 - \frac{U_{\|}}{v}\right)\sin\phi_i - U_{\perp}\cos\phi_i\right] \tag{17}$$

From equations (10) and (12), one obtains

$$U_{\perp} = \frac{\left[\frac{2k}{\Omega_0}\Phi_0 - \frac{U_{\parallel}}{v}(1+\Omega_0\tau)\right]}{\sqrt{1-\left(\frac{\Phi_0}{2kv\tau}+\frac{\Omega_0}{2kv}\right)^2}} \tag{18}$$

$$\approx \frac{\frac{\Phi_0}{2k\tau}}{\sqrt{1-\left(\frac{\Phi_0}{2kv\tau}+\frac{\Omega_0}{2kv}\right)^2}} \tag{19}$$

where we have used the fact that $U_{\parallel}/v \leq 10^{-2} \ll 1$. We approximate the Doppler shift by

$$\Omega_i \approx 2k \left| v \sin\phi_i - \frac{\frac{\Phi_0}{2k\tau}}{\sqrt{1-\left(\frac{\Phi_0}{2kv\tau}+\frac{\Omega_0}{2kv}\right)^2}} \cos\phi_i \right| \tag{20}$$

The previous approximation induces an error in the estimated Doppler given by

$$\delta\Omega_i = -2k\, U_{\parallel} \sin\phi_i - \frac{U_{\perp} U_{\parallel}}{v}(1+\Omega_0\tau)\cos\phi_i \tag{21}$$

Taking the variation of equation (17) with respect to $\delta\Phi_i$, and solving for $\delta\phi_i$, the corresponding error in the estimated azimuth angle, one obtains

$$\delta\phi_i = \frac{\left[U_{\parallel}\sin\phi_i - \frac{U_{\perp}U_{\parallel}}{v}(1+\Omega_0\tau)\cos\phi_i\right]}{v\left(1-\frac{U_{\parallel}}{v}\right)\cos\phi_i + U_{\perp}\sin\phi_i} \tag{22}$$

Therefore the fractional error in the azimuth angle is $\delta\phi_i/\phi_i \sim U/v$ which can be ignored for most applications.

Having obtained the mapping between the azimuth angles and the corresponding Doppler frequencies, we are now ready to present the VATI processing algorithm:

1. Range compress the data to the appropriate resolution and perform motion compensation corrections. In order to reduce noise, one must average looks in the range direction. This is simplest to accomplish by dividing the transmit chirp spectrum into different frequency bands and processing each band separately until the interferometric phase is estimated.

2. For each resolution cell to be processed, subdivide the returns from each channel into n groups of equal duration to be used in forming the different azimuth looks. Choose the duration of the integration time to be the smaller of the expected decor-relation time or the unfocused SAR limit integration time. Each group will be indexed by i, where $-(n - 1)/2 \leq i \leq (n - 1)/2$.

3. Select a reference Doppler, using the estimated antenna squint angle, perform Doppler sharpening using equation (4), and estimate the interferometric phase difference by multi-looking the phase differences from each range sub-band using the maximum likelihood phase estimation algorithm[19]. Use the equations derived in this section to obtain the azimuth angles, ranges, and Doppler shifts for each of the integration periods.

4. Having obtained the resolution cell's trajectory in range-Doppler space, proceed to point each synthetic aperture to the target and obtain the Doppler sharpened response. This is accomplished by interpolating the returns in range to r_i and applying equation (4).

5. Using the return from both A']'] channels form the interferogram for each angle ϕ_i, and take range looks to stabilize the estimate.

6. Estimate $U_\perp$ and $U_\parallel$ by least squares fitting equation (2).

7. Proceed to next resolution cell and repeat the process.

3. A Simple Model for the Return from a Moving Ocean

In this section, we extend the model developed in the previous section to accomodate a moving ocean surface. This model will neglect many second order effects both in the ocean hydrodynamics (small wave modulation by large waves, wave breaking, etc.) and in the scattering process (tilt modulation, multiple scattering, etc.). Nevertheless, the model is probably realistic enough to give an indication about the feasibility of the technique

proposed here.]n contrast with the usual SAR ([9], [JO], [1 1], [1 2], [13]) and ATI ([20], [21], [22]) models, the results presented here ,,, be related to physical quantities more easily due to the short integration times and the consequent absence of the non-linear aspects of wave imaging.

Provided the surface patch is small enough so that we can ignore 1)oppler variations in both range and azimuth, and using t he usual stop-start approximation for SAR modeling, the scattered field at the first ATI antenna can be modeled as:

$$E(t) = G(t)e^{-2ikr(t)}e(t) \tag{23}$$

where t is the slow time indexing the platform motion, $G(t)$ represents the weighting due to the antenna pattern, and $e(t)$ is t he scattered field from t he surface less t he factor $e^{-2ikr(t)}$, which represents the two-way propagation phase from t he radar to the patch. As in the previous section, the field at the second antenna is given by an identical expression with the exception that the field is evaluated at $(t+\tau)$.

In analog with equation (4), t he 1)oppler sharpened return is now given by

$$E_i^{(1)}(\Omega) = \frac{1}{2\pi}\int d\omega\ \hat{e}(\omega)\int_{t_i-T/2}^{t_i+T/2} dt\ W(t-t_i)G(t)e^{-2ikr(t)}e^{-i(\Omega-\omega)t} \tag{24}$$

where $\hat{e}(\omega)$ is the Fourier transform of $e(t)$. Expanding the range using equation (6), and again assuming $G(t)$ is constant over the integration interval, one of t he integrals can be evaluated. The result is

$$E_i^{(1)}(\Omega) = G_i e^{-2ikr_i}\frac{1}{2\pi}\int d\omega\ \hat{e}(\omega)\hat{W}(\Omega+2k\dot{r}_i-\omega)e^{-i(\Omega-\omega)t_i} \tag{25}$$

The effect of surface motion on the azimuth resolution factor, $\hat{W}$, is to cause frequency dependent shifts, which introduce uncertainties in the angular location of the pixel if the radial velocity is not known. The signal at t he second ATI antenna is identical, with the sole exception of an additional phase factor ('x)); i.e., $e^{-i\omega\tau}$ inside t] ie integral.

in order to calculate the mean interferometric return for the small patch, $\langle E_i^{(1)}E_i^{(2)*}\rangle$, one must make assumptions about the 1)oppler spectrum of the field scattered from the surface. In this paper, simple Bragg scattering [14] will be assumed: the return will depend

only on surface waves traveling along $\hat{N}$ $(\hat{1} - \hat{z}\hat{z})\hat{n}_i/|(\hat{1} - \hat{z}\hat{z})\hat{n}_i|$ and having wavenumber $k_B = 2k\sin\theta$, where θ is the angle of incidence (this implicitly assumes that the look direction to the scattering patch is approximately constant during the integration period). As these waves travel along the surface, they are carried along by currents due to other waves and by the mean flow of the ocean. If ω_0 is the intrinsic frequency of these waves as given by the dispersion relation, the local frequency due to Doppler shifting is given by [23]

$$\omega_B^{(\pm)} = \pm\omega_0 + k_B(\vec{U}_w + \vec{U}_c)\cdot\hat{N} \tag{26}$$

where the +/− signs apply to Bragg waves moving away or towards the radar, respectively. The surface velocity has been decomposed into a "wave" component, $\vec{U}_w$, which varies across the surface patch, and a "current" component, $\vec{U}_c$, which is assumed to be constant over the patch. One can model the scattering as being due to the incoherent addition of many small subpatches over each of which $\vec{U}_w$ is constant (this is possible since the typical scale of variation of the wave velocity is large compared to radar wavelengths). In each subpatch, the spectrum of the Doppler return will be given by

$$\left\langle \tilde{e}(\omega)\tilde{e}^*(\omega')\right\rangle = (2\pi)^2\delta(\omega - \omega')\left[\delta(\omega - \omega_B^{(+)})\sigma_0^{(+)}(k_B) + \delta(\omega - \omega_B^{(-)})\sigma_0^{(-)}(k_B)\right] \tag{27}$$

where it has been assumed that different frequency ocean waves are independent, which is a good approximation [23]. If the number of surface patches is large enough so that they are representative of the distribution of wave velocity, the Doppler spectrum for the entire patch can be written as

$$\begin{aligned}\left\langle \tilde{e}(\omega)\tilde{e}^*(\omega')\right\rangle_{(\pm)} &= (2\pi)^2\delta(\omega - \omega')\int d(k_B\hat{N}\cdot U_w)\; f(k_B\hat{N}\cdot U_w) \\ &\quad \delta\left[\left(\omega - \pm\omega_0 - k_B\hat{N}\cdot\vec{U}_c\right) - k_B\hat{N}\cdot U_w\right]\sigma_0^{(\pm)}(k_B) \qquad (28)\\ &= (2\pi)^2\delta(\omega - \omega')f\left(\omega - \pm\omega_0 - k_B\hat{N}\cdot\vec{U}_c\right)\sigma_0^{(\pm)}(k_B) \qquad (29)\end{aligned}$$

where $f(k_B\hat{N}\cdot\vec{U}_w)$ is the distribution function of the wave radial velocity, and we have separated the contributions of Bragg waves going toward or away from the radar for notational convenience. Experimentally, it has been confirmed that the Doppler spectrum does

indeed have a form very similar t o t he one derived above (see [14], for an example). The distribution function p is very close to being Gaussian for wind driven oceans at L-Band, and the Doppler bandwidth corresponds 1 o the bandwidth due to the radial wave motion,

Making these assumptions, the interferometric return is given by

$$\left\langle E_1(\Omega)E_2^*(\Omega)\right\rangle_{\pm} = G_i^2\sigma_0^{(\pm)}(k_B)\, e^{-i(\pm\omega_0 + k_B\hat{N}\cdot\vec{U}_c)\tau}\int d\omega f(\omega)\left|\hat{W}(\tilde{\Omega} - \pm\omega_0 - \omega)\right|^2 e^{-i\omega\tau} \tag{30}$$

where $\tilde{\Omega} = \Omega + 2k\dot{r}_i - k_B\hat{N}\cdot\vec{U}_c$ is the Doppler frequency corresponding to the advecting current. In the absence of big waves, $f(\omega) = \delta(\omega)$, and assuming Bragg waves moving only in one direction, the interferometric velocity for each Bragg wave component will be given by

$$v_{ATI} = \frac{\phi}{2k} = \frac{\pm\omega_0}{2k} + \hat{N}\cdot\vec{U}_c\sin\theta \tag{31}$$

The second term is recognized as the component of the current velocity along the radial direction. For gravity waves, the dispersion relation predicts that $\omega_0 = \sqrt{g2k}\sin\theta$, where g is the gravitational acceleration. Using this relation, one has that $\omega_0/2k = \sqrt{g/k_B}$ sin 0, which one recognizes as the component of the Bragg wave phase velocity in the radial direction. Hence, for an infinitely narrow Doppler spectrum, one obtains t he expected result: the ATI phase difference measures the radial component of t he velocity. 1 f Bragg waves moving in both directions are present, the ATI measured velocity will be proportional to the phase of the sum of the two returns, so that additional information about the wave spectrum (e.g., wind driven vs. isotropic. waves) is necessary in order to retrieve the velocit y (similar results for conventional ATI have been presented in [8])

Thus far, it has been assumed that the patch is narrow enough in t he direction perpendicular to the look direction that the spatial change in 1 Doppler can be neglected. In practice, the return is the sum oft he return from many independent patches located at the same range, but having different 1 Dopplershifts To obtain the interferometric signal duc to all the patches, we expand the look dir ection $\hat{n}$, shout a specific direction $\hat{n}_{i0}$. If we choose the coordinate system given by $\hat{N}_0$, $\hat{z}$, and $\hat{y} = \hat{N}_0\times\hat{z}$, t hen the di rection vector to points which lie at the same range but along the dire ction perpendicular to the look direction is

approximately given by

$$\hat{N} \approx \hat{N}_0 + \frac{p}{r_{i0}}\hat{p} \tag{32}$$

where p is the coordinate along the $\hat{p}$ direction. Similarly, it can be shown that the velocity vector to the point can be approximated by

$$\dot{r}_i \approx \dot{r}_{i0} + \frac{\partial \dot{r}_{i0}}{\partial \hat{r}_{i0}} \cdot \hat{p} = \dot{r}_{i0} + v_p \frac{p}{r_{i0}} \tag{33}$$

where we have defined v_p to be the platform velocity along the $\hat{p}$ direction. Replacing the previous two equations in equation (30), and integrating over p, one obtains the following expression for the interferometric return

$$\begin{aligned}\left\langle E_1(\Omega)E_2^*(\Omega)\right\rangle = {} & 2\pi r_{i0} G_i^2 e^{-ik_B \hat{N}_0 \cdot \hat{U}_{c\tau}} e^{i\Omega\tau\eta/(1-\eta)} w\left(\frac{-\eta\tau}{1-\eta}\right) \int d\omega f(\omega)\, e^{-i\omega\tau/(1-\eta)} \\ & \left[\sigma_0^{(+)}(k_B)\, e^{-i\omega\tau/(1-\eta)} + \sigma_0^{(-)}(k_B)\, e^{+i\omega\tau/(1-\eta)}\right]\end{aligned} \tag{34}$$

where $w(t)$ is the inverse Fourier transform of $|W(\omega)|^2$, and we have introduced $\eta = U_c \cdot \hat{p}/v_p$, the ratio of the components of the current and platform velocities perpendicular to the look direction. Typically, one has that $\eta \ll 1$.

The integral in equation (34) is the Fourier transform of the scattered field Doppler spectrum, i.e., it is proportional to the field time covariance function, $C(t)$. Furthermore, since $f(\omega)$ has been assumed to be a probability density function, $C(0) = 1$, and the integral is in fact the scattered field correlation function. The final result for the complex interferometric correlation function, γ, is given by

$$\gamma \equiv \frac{\left\langle E_1(\Omega)E_2^*(\Omega)\right\rangle}{\sqrt{\left\langle |E_1(\Omega)|^2\right\rangle \left\langle |E_2(\Omega)|^2\right\rangle}} = \gamma_\tau \gamma_N \tag{35}$$

$$\gamma_\tau = \frac{e^{-ik_B \hat{N}_0 \cdot \hat{U}_{c\tau}} e^{i\Omega\tau\eta/(1-\eta)} \left[\sigma_0^{(+)} e^{i\omega\tau/(1-\eta)} + \sigma_0^{(-)} e^{+i\omega\tau/(1-\eta)}\right]}{\left[\sigma_0^{(+)} + \sigma_0^{(-)}\right]} \times \frac{w\left(\frac{-\eta\tau}{1-\eta}\right) C\left(\frac{\tau}{1-\eta}\right)}{w(0)} \tag{36}$$

$$\gamma_N = \frac{1}{\sqrt{1+\mathrm{SNR}_1^{-1}}\sqrt{1+\mathrm{SNR}_2^{-1}}} \tag{37}$$

Where, $\tilde{\Omega} = \hat{\Omega} \pm \omega_0$. in addition to the signal decorrelation, the effect of thermal noise decorrelation in both channels has also been included [16]. The total cot-relation is the product of the signal correlation function times, γ_τ, and the noise correlation function, γ_N. The phase of γ is used to obtain the interferometric velocity, while the magnitude of γ governs the variance of the phase (i.e., velocity) estimate [19].

The effect of the finite signal bandwidth is to make the measurement cor relation function dependent on the field correlation function, as one would expect intuitively. The effect of having both forward and backwards travelling waves is to introduce a phase shift and decrease the magnitude of the correlation function One can write the cross sect ion-dependent part of γ_τ as

$$\sqrt{\cos^2\left(\frac{\omega_0\tau}{1-\eta}\right) + \left(\frac{\sigma_d}{\sigma_s}\right)^2 \sin^2\left(\frac{\omega_0\tau}{1-\eta}\right)} \exp\left(-i\tan^{-1}\left[\left(\frac{\sigma_d}{\sigma_s}\right)\tan\left(\frac{\omega_0\tau}{1-\eta}\right)\right]\right)$$

where σ_s and σ_d are the sum and difference of the forward and back propagating cross sections, respectively. This shows that when both forward and backward traveling waves are equal in magnitude, there is a decrease in the correlation function by a factor of $\sim \cos\omega_0\tau$, while the velocity measured corresponds solely to the current velocity. Depending on the ratio σ_d/σ_s, it is possible to add any phase in the range $\pm\omega_0\tau$ to the estimated ATI phase. Additional information, such as the variation of the velocity as a function of incidence angle, must be used in order to separate the two effects.

The length of the integration period also contributes to the decorrelation of the two fields through the $w(-\eta\tau/(1-\eta))$ term. Its contribution will be small as long as $T >> \eta\tau$, where T is the duration of the integration period.

4. System Design Consideration

In the previous discussion, there are several parameters which are free to vary and may be chosen in order to optimize system performance. In this section we will examine two of these parameters: range resolution] and integration time.

Integration Time:

Angular resolution is obtained by interpreting Doppler shifts in terms of angle by means of the Doppler shift relation

$$\delta f = \frac{2v}{\lambda}\delta\phi \tag{38}$$

where δf is the resolution with which a signal from the scattering patch can be resolved. If one views the return signal as the product of a deterministic signal which can be resolved with resolution $\delta f_D = 1/T'$, and a finite bandwidth random signal whose correlation time is $1/\tau_c$, then the angular resolution possible is given by [13]

$$\delta\phi = \frac{\lambda}{2v}\langle(\delta f)^2\rangle \approx \frac{\lambda}{2v}\sqrt{\frac{1}{T^2} + \frac{1}{\tau_c^2}} \tag{39}$$

It is clear from this equation that the maximum angular resolution which can be achieved is given by $\delta\phi_{max} = \lambda/(2v\tau_c)$ and that integrating for times much longer than the correlation time does not increase the angular resolution significantly.

Another restriction on the integration time is given by the requirement that the range curvature term, which was ignored in equation (6), contributes only a small factor to the return phase

$$\frac{\pi}{4} > k\ddot{r}_i\left(\frac{T}{2}\right)^2 = k\frac{v^2\cos^2\phi}{r_i}\left(\frac{T}{2}\right)^2 \tag{40}$$

Hence, the requirement on the integration time is given by

$$\frac{1}{v\cos\phi}\sqrt{\frac{\lambda r_i}{2}} > T \tag{41}$$

where ϕ is the azimuth angle. Figure 3a presents the limits set by the integration time on the JPL AI RSAR L-Band ATI system as a function of incidence angle. This value should be compared against the typical correlation times for the ocean at L-Band, which are in the 0.05-0.25 second range [16].

A further restriction on the integration time is derived from the term $w_{\left(\frac{-\eta\tau}{1-\eta}\right)}$ in equation (36), which implies that in order to maximize the correlation, it is desirable that $T >> \eta\tau$. This is not a very stringent requirement since for the JPL AIRSAR ATI, τ = 0.0 94sec or τ = 0.047sec, depending on whether both antennas transmit or only one transmits, respectively [16].

A final consideration in choosing the integration time is that by decreasing the integrating time, one increases the number of angles which can be used in fitting for the velocity vector, at the expense of spatial resolution. However, for a given resolution and as long as the number of looks is large enough, it is equivalent to trade one quantity for the other since the noise reduction by a factor of $N^{1/2}$ is the same whether one takes the looks in angle or real space..

Given all the previous considerations, it seems appropriate to choose an integration time on the order of $\sim$ 0.1 seconds for the ,1} '1, AIRSAR L-Band ATI system.

Range Resolution:

Two considerations put restrictions on the desired range resolution: one wishes to have a coarse range resolution (of the same order of magnitude as the azimuth resolution) in order to have to avoid making range migration corrections; on the other hand, if the range cell is too large, points at the two extremes of the cell may have significantly different Doppler shifts, which will cause defocusing,.

The amount of range migration within the integration time T is given by

$$\Delta r_i = vT \sin\phi \tag{42}$$

If the range resolution is denoted by R, and I we require that the range migration be smaller than 1/10 the range resolution, one derives the following restriction on the range resolution

$$R > 10vT \sin\phi \tag{43}$$

For the JPL AIRSAR parameters, an integration time of 0.1 see, and an azimuth angle of 3°, this implies that the range resolution must be greater than $\sim$ 11 m

The interferometric phase difference over an integration period, Φ, can be written in terms of the incidence angle, O, and the azimuth angle in the x-y plane, α, as

$$\Phi = 2k\hat{r}_i \cdot \vec{vT} = 2kvT \sin\alpha \sin\theta \tag{44}$$

Taking the derivative of this quantity with respect to θ, using the fact that $\delta\theta =$ R tan θ/r_i, and requiring that the interferometric phase difference during the integration interval and

across the resolution cell be less than $\pi/4$, one derives the following restriction on the range resolution

$$R < \frac{z''}{8k_0 T \sin\alpha \sin\theta} \tag{45}$$

Figure! *3b shows* the maximum range resolution allowed, given the maximum allowed integration time. Recalling that the across track resolution is related to the range resolution by a factor of 1/ sin θ, one sees that, given the desired spatial resolutions, there is no major practical restriction on the degradation of range resolution allowed to minimize range walk and to minimize the interpolation of the data. This is also advantageous in that one may take looks by subdividing the return chirp spectrum in the frequency domain to obtain independent looks of the same range cell which are colocated.

5. Measurement Accuracy

Random Errors:

A Monte Carlo experiment was performed in order to test the accuracy of the technique outlined above as a function of the surface velocity magnitude and orientation. The major source of measurement error is due to the loss of correlation between the two ATI channels, For each azimuth angle, N_r ATI measurement pairs were simulated by generating pairs of circular Gaussian random numbers of given correlation and shifted in phase relative to each other as in equation (2). Using these data, the interferograms were computed, averaged over all the range samples, and the interferometric phase was estimated. Finally, the vector velocity was estimated by least squares fitting. This process was repeated 103 times in order to obtain stable estimates for the errors and means.

We present the results here in terms of the normalized velocity $U' \equiv U/(\lambda/\tau)$. Figure 4 presents a conversion table between normalized velocity and true surface velocity for the various JPL AIRSAR ATI configurations. Three magnitudes of the normalized surface velocity were examined, U' = 0.05, *0.1,* 0.2, and the surface velocity direction was allowed to point at 0°, 45", and 90° relative to the antenna boresight direction. Notice that when the velocity vector points along the look direction, a normalized velocity of 0.2 corresponds

standard deviation can be approximated by its Cramer-Rao bound, which is given by [19],

$$\sigma_{\phi} = \frac{1}{\sqrt{2N}} \frac{\sqrt{1-\gamma^2}}{\gamma} \tag{48}$$

The solid lines in Figure 7 represent the result of replacing equation (48) in equation (47). There is good agreement between the analytic and the simulation results, so that the accuracy of the velocity vector can be estimated for arbitrary measurement configurations.

Translating the results in Figure 7 into real velocities by using Figure 4, we see that it is possible in principle to measure the HH1:111('1 component of the velocity to an accuracy which is on the order of 10cm/s on a spatial scale of 65m x 65m. This is accuracy is already of oceanographic interest at spatial scales much smaller than those required by most oceanographic applications. Since the velocity error will decrease linearly with the resolution cell size, this implies that velocity measurements of the order of 1cm/s accuracy can be obtained by averaging to spatial scales on the order of $(0.5\text{km})^2$

Motion **Compensation** Errors:

A detailed discussion of motion compensation issues is beyond the scope of this paper, and will be discussed elsewhere (Jmeland Rodríguez, in preparation). Here, we present results which are applicable under the conditions assumed in Appendix B.

The primary effect of uncompensated motion errors will be on the interferometric phase, with secondary (negligible) effects on the synthetic aperture pointing. We model the interferometric phase return with motion compensation errors as $\Phi_i' = \Phi_i + \Phi_i^{(m)}$, where the last term represents the phase due to uncompensated motion in the look direction. For short integration times, we model the motion compensation phase error as

$$\Phi_i^{(m)}(t) = 2k\left[s_0 + \dot{s}t + \frac{1}{2}\ddot{s}t^2\right] \tag{49}$$

In the limit of many observations, one can replace the summations in equations (61) and (62) by integrals. The errors due to motion compensation can then be written as

$$\delta U_{\perp} = \frac{1}{2k\tau} \frac{1}{T_a} \int_{-T_a/2}^{T_a/2} dt\ \Phi_i^{(m)}(t) = \frac{1}{\gamma}\left[s_0 + \frac{1}{24}\ddot{s}T_a^2\right] \tag{50}$$

$$\delta U_{\parallel} = \frac{1}{2k\tau} \frac{\rho_0}{v} \frac{\int_{-T_a/2}^{T_a/2} dt\ t\Phi_i^{(m)}(t)}{\int_{-T_a/2}^{T_a/2} dt\ t^2} = \frac{1}{\gamma}\frac{\ddot{s}T_a}{\phi_B} \tag{51}$$

where T_a is the total time used to observe the target while forming the velocity vector estimate. These equations show that the perpendicular component of the velocity is sensitive to the mean uncompensated path and the radial acceleration; the parallel component, on the other hand, is sensitive to uncompensated radial velocities. The presence of the $1/\phi_B$ factor in the denominator of equation makes the parallel component much more sensitive to residual motion errors than the perpendicular component.

An additional systematic source of error is due to misregistration between the two images. Since misregistration leads to an apparent motion of one image relative to the other, can also lead to errors in the estimated velocity. If δx is the range or azimuth misregistration, the induced error error in either component of the velocity is given by

$$\delta U = \frac{\delta x}{\eta} \tag{52}$$

Where $U = U_\perp$ when δx is a range misregistration, and $U = U_\parallel$ when δx is an azimuth misregistration. This type of misregistration is present if the interferometric baseline or the aircraft velocity are estimated incorrectly.

6. VATI Demonstration Using the JPL AIRSAR Instrument

In this section, we briefly present results of applying the VATI algorithm described here to interferometric radar data acquired using the L-band JPL AIRSAR ATI configuration [16]. A fuller description of the details of the processing will be presented separately (Imel and Rodriguez, in preparation).

The data used here was collected over the Currituck Sound (North Carolina) which lies north of Kitty Hawk Beach, the Albemarle Sound, and Cape Hatteras (see Figure 8), The JPL AIRSAR ATI instrument flew in the south-east direction, roughly following the western coast of the sound. L-band ATI data were collected and processed using VATI processing. Unfortunately, we have no ground-truth data for this site Due to the enclosed nature of the Sound, however, we assume that flow in the Sound must be dominated by tidal currents, which must be roughly parallel to the Sound axis. Inhomogeneities in the observed currents can be due to interaction with the boundaries, or with bottom topography. The

south-eastern section of the processed image also contains data from a coastal region on the Atlantic Ocean. We expect the wave height in the sound to be low (with corresponding high temporal correlation times). By contrast, we expect significant wave motion in the shoaling region of the Atlantic Ocean, leading to shorter temporal correlation. We emphasize that, due to the absence of ground truth data, these are merely speculations based on "typical" conditions.

Figure 9 presents the estimated vector velocities after averaging of the results over approximately (300m)2. The image brightness is the unfocused SAR image of the region after equalization by a ramp in the range direction to compensate for incidence angle variations. In this image, land can be seen as bright features in the upper right hand (south-east) and lower left hand (north-west) corners. The dark patch in the south-east corner represents returns from the small bay shown in Figure 8. In addition to the land returns, there are modulations in the returns from the water which can be as in-sight as the returns from the land as well as lesser-modulations. It is not known whether these modulations are due to bathymetric modulation of the wave spectrum or to local wind gusting.

The vector velocities in Figure 9 show coherent structures in range and azimuth. A possibly spurious effect is the modulation bands in the parallel velocity which are visible from near to far ranges, perpendicular to the airplane heading. This modulation is most clearly visible at a distance of ~20km along track. Since these bands have signatures in both water and land, and for all ranges, they may be due to uncompensated motion (details on the motion compensation used are will be presented by Imel and Rodríguez, in preparation).

Figure 10 shows a histogram for the two components of the velocities shown in Figure 9. These velocities are consistent in order of magnitude with expected current velocities for both the range and azimuth directions, although the along track component shows greater estimation noise. The magnitude of the perpendicular component, on the other hand, shows a hard limit in the histogram due to wrap around effects of the phase difference and could be potentially be removed using a phase unwrapping algorithm [24]. As expected, most of the current is parallel to the Sound axis, which changes from being at a slight angle to the

flight direction, in the beginning of the pass, to being almost perfectly aligned with the track direction in the western bounds-y, t owards the end of the pass (see Figure 8). The largest coherent feature of the current is a strong component which is very nearly tangential to the eastern boundary of the Sound. There is also a strong component loacated at about 5km along-track: it is not clear whether this is an artifact, or can be attributed to wind gusting or the narrowing of the Sound at the northern boundary of the data take. Since the velocity increase is only present in a small section of the water, and not through all ranges, it is not very likely that it can be attributed to motion compensation errors. We note the presence of coherent, velocity patches which are inhomogeneously distributed in the range direction, again arguing against motion compensation errors. These velocity modulations sometimes coincide with brightness features (southern part of the run), but are sometimes present without any perceivable surface manifest a tion. Finally, we note the shoaling zone current seems to be significantly noisier than the velocities in the Sound. This is probably duc to the presence of strong wave motion or t rue current variability. Nevertheless, the shoaling current seems to follow the shoreline closely, in agreement with intuitive expect at ions. Finally, we note the presence of non-zero velocities over some of the land regions. The largest vectors seem quite noisy and appear to be directed against the main flow di rcct ion s. whether there is a physical mechanism due to these veloc i tics, or whether they are measurement artifacts, is an open issue.

7. Conclusions

We have presented a new technique for measuring vector velocities from moving ocean surfaces using the angular diversity provided by the azimuth beamwidth of the ATI instrument. We also presented a physical scattering model for the measured velocity showing the contribution of current and Bragg wave velocit ies to the final measured velocities. System and processor issues were also add ressed, arid sensitivity equations were der ived for both components of the velocity. These equat ions agreed well with a simulation of the measurement. Using the parameters for t he JPL A 1 RSA R i] ist r ument, we showed that useful measurements of the surface velocit y could be m rode, provided spat ial averaging over a few

hundred meters was performed. We also analyzed the effects of uncompensated motion, and showed that this may be the dominant contributor to systematic errors in the parallel component of the velocity. To demonstrate the technique, we processed data taken over the Currituck Sound (North Carolina), and showed that the measured velocities showed coherent effects which were not inconsistent with physical expectations. However, due to the lack of ground truth, these observations could not be verified. We conclude that the technique presented here is potentially very useful for ocean current measurements. To make the technique viable will require very good platform motion measurements. We believe that these measurements are currently becoming feasible with the use of differential GPS coupled with accurate inertial navigation units.

Appendix A

In this appendix we present the idea behind the ATI algorithm from a spectral perspective. The range history of the point target as viewed from the first antenna is given by

$$r_1(t) = \sqrt{(\rho_0 - U_\perp t)^2 + \left[(v - U_\parallel)t\right]^2} \tag{53}$$

After making a translation to account for the displacement between the two antennas, the range from the second antenna to the target is given by

$$r_2(t) = \sqrt{(\rho_0 \rho_0 (t + \tau)U_\perp)^2 + \left[(v - U_\parallel)t - U_\parallel \tau\right]^2} \tag{54}$$

Had there been no perpendicular component to the velocity, then one would have that $r_2(t) = r_1(t - \delta t)$, where $\delta t = U_\parallel \tau / (v U_\parallel)$ corresponds to a constant time shift between the two signals. When $U_\perp \neq 0$, the relationship is no longer exact, but can be approximated by

$$r_2(t) \approx r_1(t - \delta t) - U_\perp \tau \left(1 - \frac{U_\parallel}{v - U_\parallel}\right) \frac{\rho_0}{r_1(t - \delta t)} \tag{55}$$

So that, in this approximation, the phase history for the second point target is equal to the a time shifted version of the phase shift for the first target multiplied by a phase proportional

to the perpendicular component, of t he velocity. The Fourier t ransform of the signal from the second antenna will then be given by

$$E_2(\Omega) = \int dt\ G(t) \exp\left[-2ikr_1(t-\delta t)\right] \exp\left[2ikU_\perp \tau \left(1 - \frac{U_\parallel}{v - U_\parallel}\right) \frac{\rho_0}{r_1(t-\delta t)}\right] e^{-i\Omega t} \quad (56)$$

where $G(t)$ is the antenna pattern. Making a change of variables, and applying the usual stationary phase approximation] [18], one finds

$$E_2(\Omega) = \exp\left[2ikU_\perp \tau \cos\phi\right] e^{i\Omega\delta t} E_1(\Omega) \quad (57)$$

where a term of order $U_\parallel/v$ has been neglected in the perpendicular velocity term. Using the fact that at the stationary point one can write $\Omega = 2k(v - U_\parallel)\sin\phi$, we can write the cross product of the two Fourier transforms as

$$E_1(\Omega)\,(E_2(\Omega))^* = |E_1(\Omega)|^2 \exp\left[-2ik\tau\left(U_\parallel \sin\phi + U_\perp \cos\phi\right)\right] \quad (58)$$

which is identical to the result obtained using t he geometrical approach

The additional insight afforded by t 1, esecond approach is t hat one recognizes that estimating the parallel velocity component is equivalent to estimating a shift in the two interferometric images in the along track direction by the amount $U_\parallel \tau$. This point of view can also give rise to different implementations of the algorithm presented here. For instance, if one uses conventional SAR methods to form the two images, t hen t he perpendicular component can be measured by estimating the phase difference between the two images, while the parallel components can be measured by finding the optimal along track shift between the images. This along t] ack shift could be measured by local estimation of the along-track correlation peak.

APPENDIX B

In this appendix we derive the expected standard deviation of t he velocities assuming that the beamwidth is small, and t he looks are uniformly sampled in angular space and are symmetric relative! to the broadside direction

In the small angle approximation, the interferometric phase can be written as

$$\Phi_i \approx 2k_r \left(U_{\parallel} \phi_i + U_{\perp} \right) \tag{59}$$

Assuming uniformly spaced synthetic apertures we can write

$$\phi_i \approx \frac{vt_i}{\rho_0} = i \frac{v\Delta t}{\rho_0} \tag{60}$$

for $-(N_{az} - 1)/2 \leq i \leq (N_{az} - 1)/2$. It is easy to show that the least square estimate for the velocities is then given by

$$U_{\perp} = \frac{1}{2k_r} \frac{1}{N_{az}} \sum_i \Phi_i = \frac{1}{2k_r} \frac{1}{N_{az}} \langle \Phi \rangle \tag{61}$$

$$U_{\parallel} = \frac{1}{2k_r} \frac{\rho_0}{v\Delta t} \frac{\sum_i i \left(\Phi_i - \langle \Phi \rangle \right)}{\sum_i i^2} \tag{62}$$

Assuming that the variations of the interferometric phase about the mean satisfy

$$\langle \delta\Phi_i \delta\Phi_j \rangle = \delta_{ij} \sigma_{\Phi}^2 \tag{63}$$

the variance of the estimated velocities are given by

$$\sigma_{U_{\perp}} = \frac{1}{2k_r} \frac{\sigma_{\Phi}}{\sqrt{N_{az}}} \tag{64}$$

$$\sigma_{U_{\parallel}} = \frac{1}{2k_r} \frac{\sqrt{12}}{\phi_B} \frac{\sigma_{\Phi}}{\sqrt{N_{az}^2 - 1}} \tag{65}$$

where $\phi_B = v\Delta t N_{az}/\rho_0$, is the processing beamwidth.

ACKNOWLEDGEMENTS

The research described in this paper was performed by the Jet Propulsion Laboratory, California Institute of Technology, and was jointly sponsored by ONR, through an agreement with the National Aeronautics and Space Administration. We would like to acknowledge useful discussions with Richard Carande, Yunjin Kim, Scott Hensley, and Paul Rosen. We would also like to acknowledge Yunling Lou and Leon Maldonado for help in providing us with the radar data.

References

[1] R. Goldstein and H. Zebker, "Interferometric radar measurement of ocean surface currents," *Nature*, vol. 328, no. 20, pp. 707-709, 1987.

[2] M. Mar-cm, R. Goldstein, E. Thornton, and L. Shemer, "Remote sensing of ocean wave spectra by interferometric synthetic aperture radar," *Nature*, vol. 345, no. 28, pp. 793--795, 1990.

[3] M. Marom, L. Shemer, and E. Thornton, "Energy density directional spectra of nearshore wave field measured by interferometric synthetic aperture radar,)' *J. Geophys. Res.*, vol. 96, no. C12, pp. 22,125-27,134, 1991.

[4] R. Goldstein, F. Li, J. Smith, R. Pinkel, and T. Barnett, "Remote sensing of ocean waves: The surface wave process program experiment," *J. Geophys. Res.*, vol. 99, no. C4, pp. 7945-7950, 1994.

[5] T. Ainsworth, S. Chubb, R. Fusina, R Goldstein, R. Jansen, J. Lee, and G. Valenzuela, "INSAR imagery of surface currents, wave fields, and fronts," *IEEE Trans.* Geoscience *and Rem. Sens.*, *vol.* 33, no. 5, pp. 1117-1123, 1995.

[6] R. Goldstein and T. Barnett, "Remote sensing of ocean currents," *Science*, vol. 246, pp. 1282-1285, 1989.

[7] L. Shemer, M. Marom, and D. Markman, "Estimates of currents in the nearshore ocean region using synthetic aperture radar," *J Geophys. Res.*, vol. 98, no. C4, pp. 7001-*7010, 1993.*

[8] D. Thompson and J. Jensen, "Synthetic aperture radar interferometry applied to ship-generated internal waves in the 1989 Loch Linhe experiment," *J. Geophys. Res.*, vol. 98, no. C6, pp. 10,259-10,269, 1993.

[9] K. Hasselman, R. Raney, P. W.J., W. A lpers, R. Shuchman, 11. Lyzenga, C. Ruffenach, and M. Tucker, "Theory of synthetic aper lute radar ocean imaging: a MARSEN view," *J. Geophys. Res.*, vol. 90, no. C3, pp. 4659 4686, 1985.

[10] D. Kasilingam and O. Shemdin, "Theory for synthetic aperture radar imaging of the ocean surface: with an application to the tower ocean wave and radar dependence experiment on focus, resolution, and wave height spectra," *J. Geophys. Res.*, vol. 93, no. C11, pp. 13,837-13,848, 1988.

[11] D. Lyzenga, "An analytic representation of the synthetic aperture radar image spectrum for ocean waves," *J. Geophys Res.*, vol. 93, pp. 13,859 13,865, 1988.

[12] R. Raney and P. Vachon, "Synthetic aperture radar imaging of ocean waves from an airborne platform: focus and track impissues," *J. Geophys. lies.*, vol, 93, pp. 12,475–12,487, 1988.

[13] D. Kasilingam and O. Shemdin, "Models for synthetic aperture radar imaging of the ocean: a comparison," *J. Geophys. Res.*, vol 95, no. C9, pp. 16,263 16,276, 1990.

[14] W. Keller and W. Plant, "Evidence of bragg scattering in microwave doppler spectra of sea return," *J. Geophys. Res.*, vol 95, no. C9, pp. 16,299 16,310, 1990.

[15] 1,. Shemer and M. Marom, "Estimates of ocean coherence time by an interferometric SAR," *Int. J. Remote Sensing*, vol 1 4, no. 16, pp. 3021-302'9, 1993.

[16] R. Carande, "Estimating ocean coherence time using dual-baseline interferometric synthetic aperture radar," *IEEE Trans. Geoscience and Rem. Sens.*, vol. 32, no. 4, pp. 846-854, 1994.

[17] S. Madsen, "A dual aspect angle along track interferometer (JOM 3348.9(} 100)," tech. rep., Jet Propulsion Laboratory, 1 'asadena, CA 91109, 1990.

[18] J. Curlander and R. McDonough, *Synthetic Aperture Radar: Systems and Signal Processing*, Wiley-Interscience, 1991.

[19] E. Rodriguez and J. M. Martin, "Theory and design of interferometric synthetic aperture radars," *IEE Proc.-F*, *vol.* 139,no2,pp. 147-159, 1992.

[20] L. Shemer and E. Kit, "Simulation of an interferometric synthetic aperture imagery of an ocean system consisting of a current and a monochromatic wave, " *J. Geophys. Res.*, vol. *96,* no. C12, pp. 22.,063 22,073, 991.

[21] L. Shemer, "An analytical presentation of the monochromatic ocean wave image by a regular or an interferometric synthetic aperture radar," *IEEE Trans. Geoscience and Rem. sells.*, vol. *33,* no. *4,* pp. 1008 1013, I 995.

[22] L. Simmer, "on the focusing of (ma!) swell images produced by a regular and by an interferometric SAR," *Int. J. Remote Sensing,* vol. 16, no. 5, pp. 925 947, 1995.

[23] *0.* Phillips, *The Dynamics of the Upper Ocean.* Cambridge University Press, *197'7,*

[24] *R.* Goldstein, H. Zebker, and C. Werner, "Satellite radar interferometry: Two-dimensional phase unwrapping," *Radio Science,* vol. *23,* no. *4,* pp. *713-720, 1988,*

TABLES

Parameter	C-Band	L-Band
Wavelength (cm)	5.7	24.0
Azimuth Beamwidth (deg)	2.5	8
Nominal Altitude (km)	8.2	8.2
Nominal Velocity (m/s)	215	215
Along-Track Spacing (m)	1.9	19.8
Along-Track Spacing (wavelengths)	38	82
Nominal Revisit Times (msec)	45/90	47/94

Table 1: Parameters for the JPL AIRSAR ATI instrument. To maximize measurement sensitivity, the L-band configuration with the longer revisit time was used in this paper.

REFERENCES

FIGURE CAPTIONS

Figure 1: Conceptual diagram of the measurement concept for the VATI technique. The intervals between tick marks along the flight path represent the segments of data used to form the synthetic beams (dashed lines) pointed at the surface patch in the direction $\hat{n}(\phi)$, where ϕ is the azimuth angle. Each interferometric measurements is proportional to the velocity vector projected on the look direction.

Figure 2: For stationary targets there exists an approximately linear relationship between the azimuth angle, ϕ, and the Doppler shift, Ω (dashed line). When the target moves, this relationship is shifted by $\Phi/\tau \approx 2k U_\perp \cos\phi$, where Φ is the interferometric phase difference and τ is the revisit time. Since Φ can be measured independently of Ω, the relationship between ϕ and Ω can be established (solid line).

Figure 3: (a) Maximum integration time allowed for unfocused SAR processing for the JPL AIRSAR L-Band system. (b) Largest range resolution allowed by the restriction that the Doppler signatures from the front and back of the range pixel have the same Doppler signature. The azimuth angle was assumed to be 3.5° for both cases.

Figure 4: Conversion table between true radial velocity and normalized velocity.

Figure 5: (a) Dwell time of a 7° antenna as a function of incidence angle. The nominal 3dB beamwidth of the JPL AIRSAR L-Band antenna is 8°. (b) Number of look angles per dwell time and incidence angle given an unfocused SAR integration time of 0.1 sec.

Figure 6: (a) Azimuth resolution as a function of incidence angle for a 0.1 second integration time. (b) Number of range looks per azimuth resolution cell as a function of incidence angle, and assuming a 40MHz chirp bandwidth.

Figure 7: Estimated standard deviation of the parallel component of the radial velocity from Monte Carlo simulations (symbols) and theory (solid line). The velocity vector can point along the broadside direction, $\phi = 0°$, at 45 degrees to the look direction, $\phi = 45°$, or along the velocity vector, $\phi = 90°$. The normalized magnitudes of the velocity were 0.2 (+), 0.1 (0), or 0.05 (A).

Figure 8: Map of the Currituck Sound region in North Carolina The SAR swath is

approximately given by the parallelogram in the middle of Currituck Sound.

Figure 9: Estimated vector velocities for the Currituck Sound data The unfocused SAR image is presented to help separate ocean and land returns. '1 'he red vectors in the upper right hand corner represent 2 m/s radial and azimuth velocities. Notice that one needs to multiply the slant range by a factor 1 / $\sin\theta \approx 2$, where θ is the incidence angle, to go from slant range to ground spacing in the range direction

Figure? 10: Normalized histograms of the parallel (solid line) and perpendicular (dashed line) velocity components fo the Currituck Sound data set.

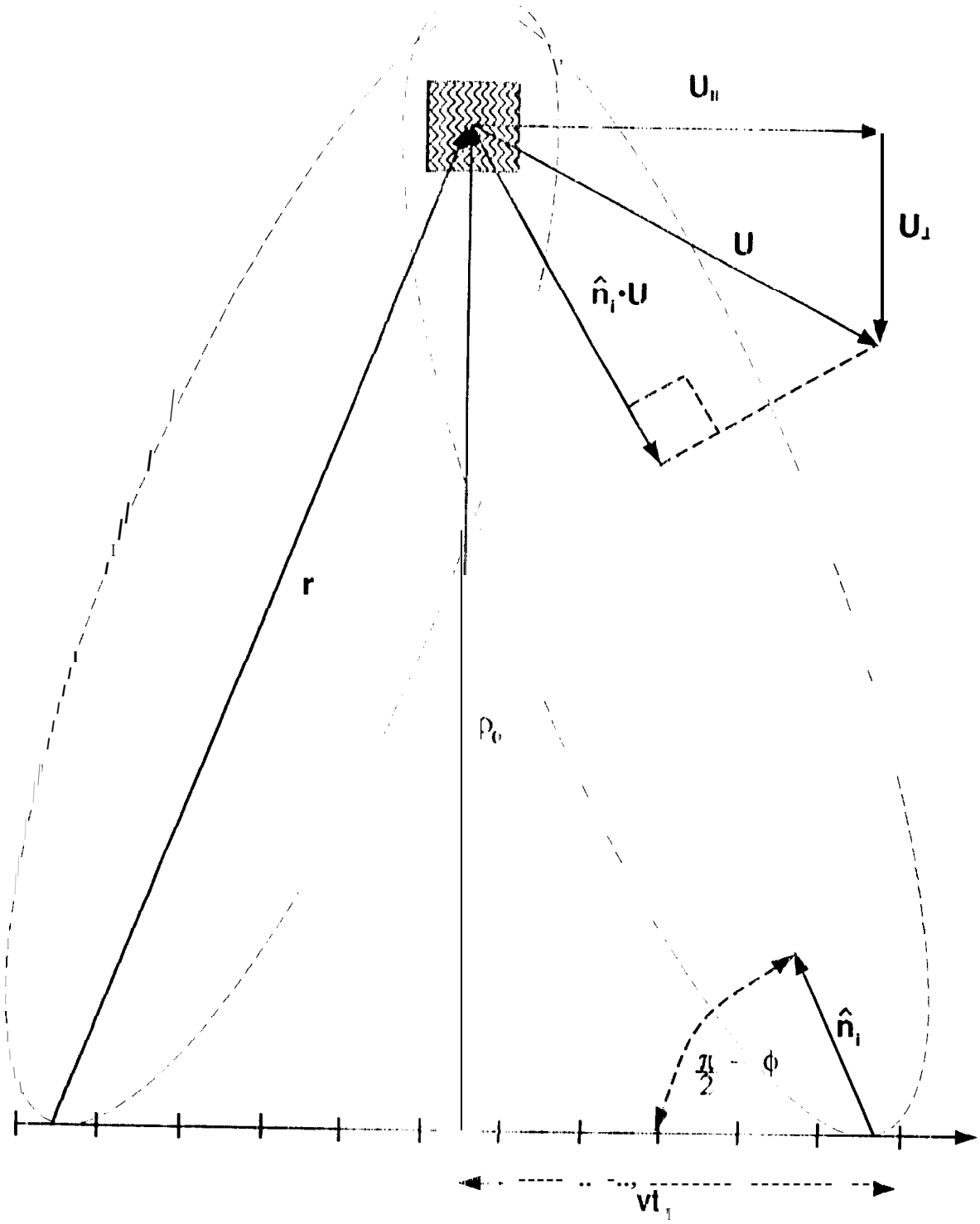

Figure 1

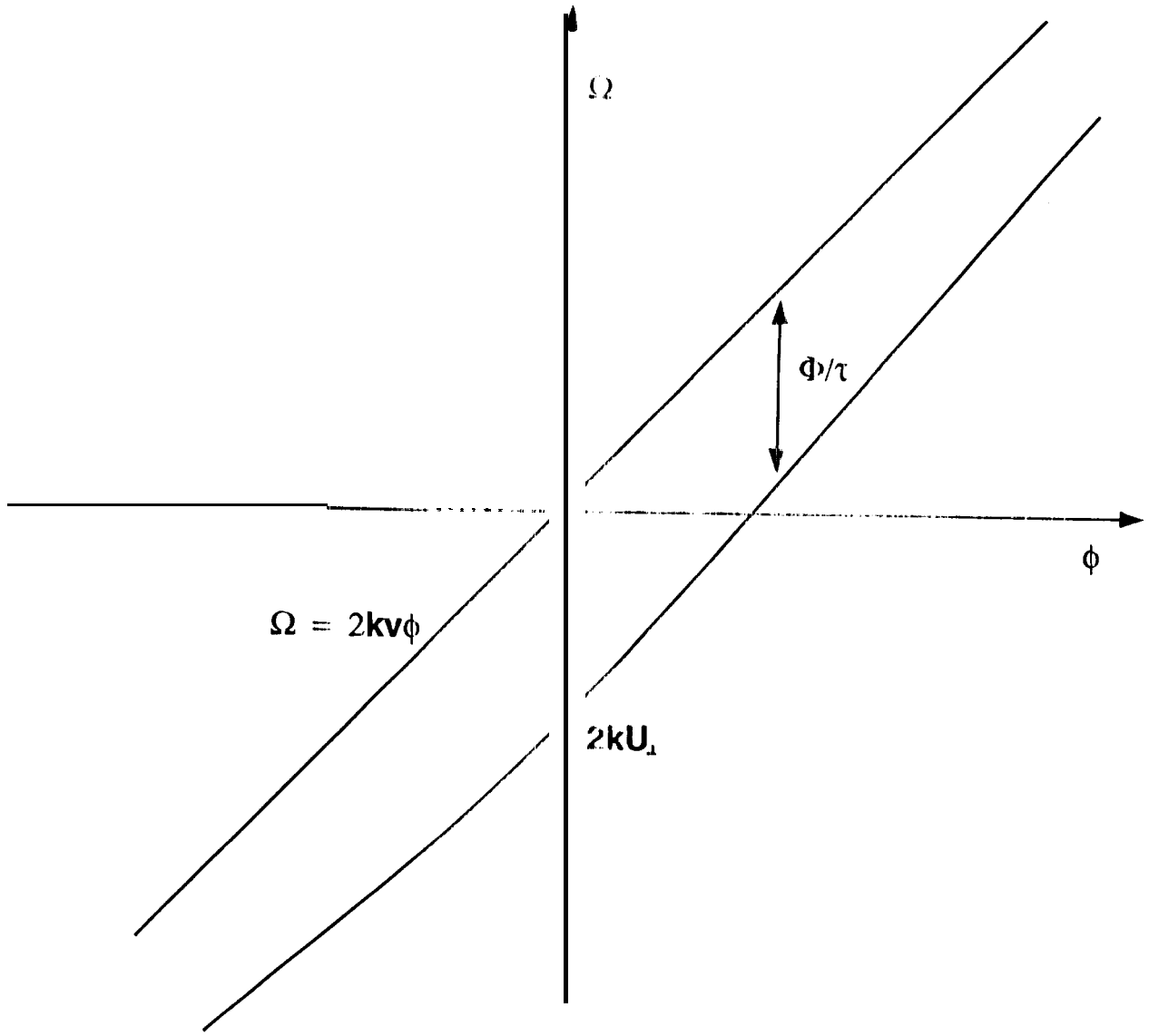

Figure 2

(a)

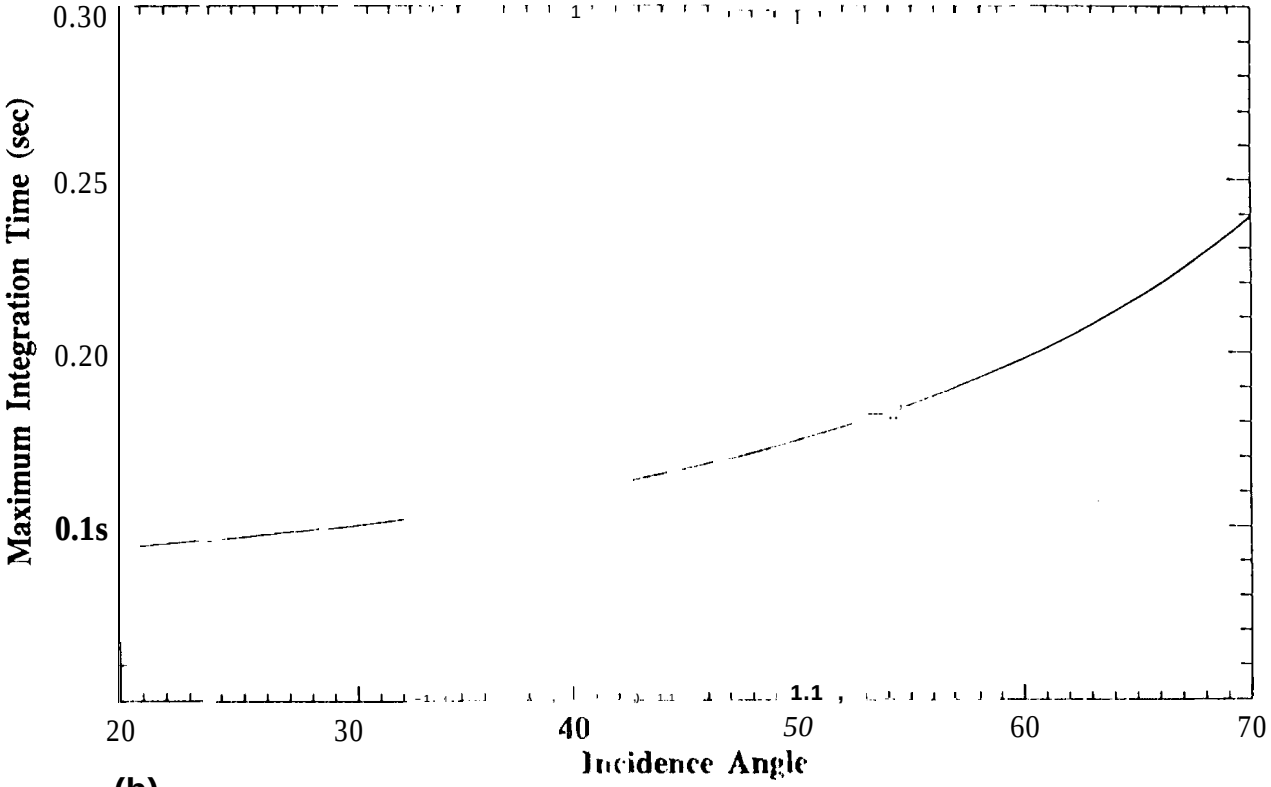
0.30
0.25
0.20
0.1s
Maximum Integration Time (sec)
20
30
40
50
60
70
Incidence Angle

(b)

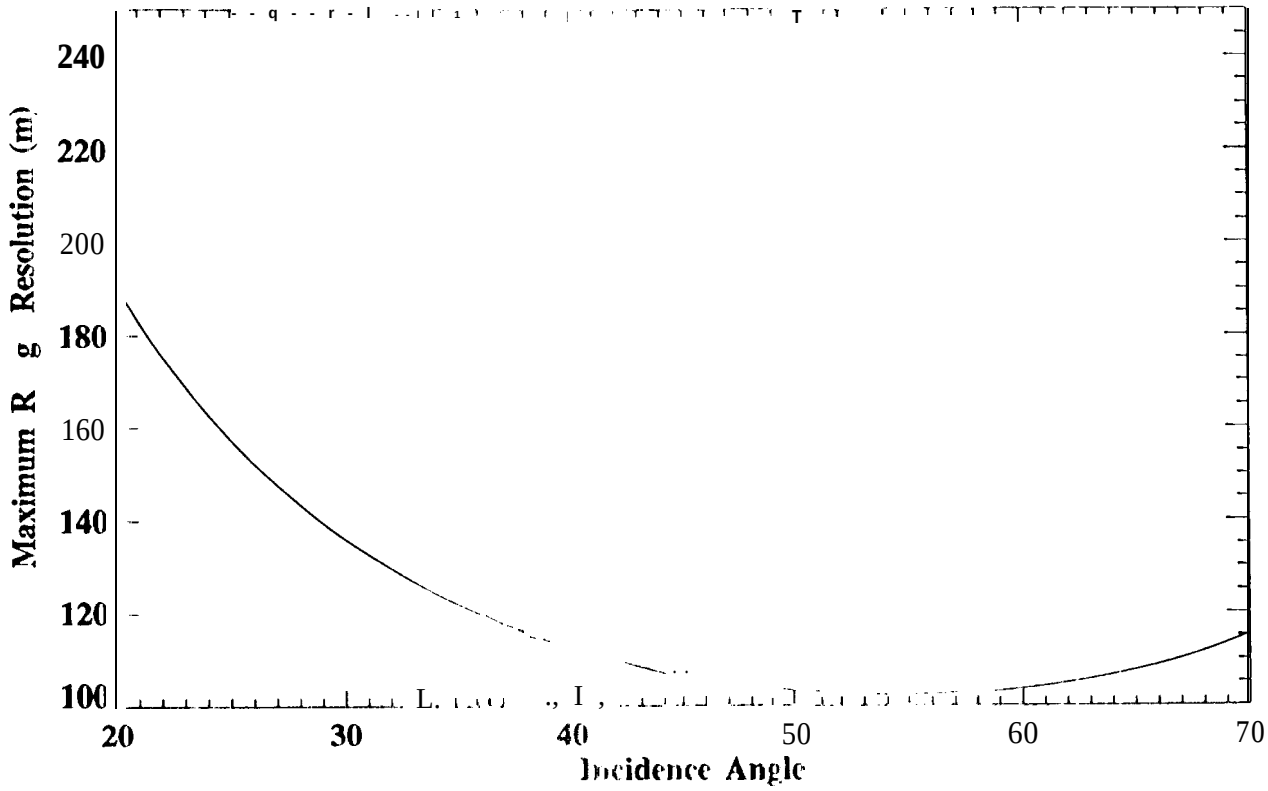
240
220
200
180
160
140
120
100
Maximum R g Resolution (m)
20
30
40
50
60
70
Incidence Angle

Figure 3

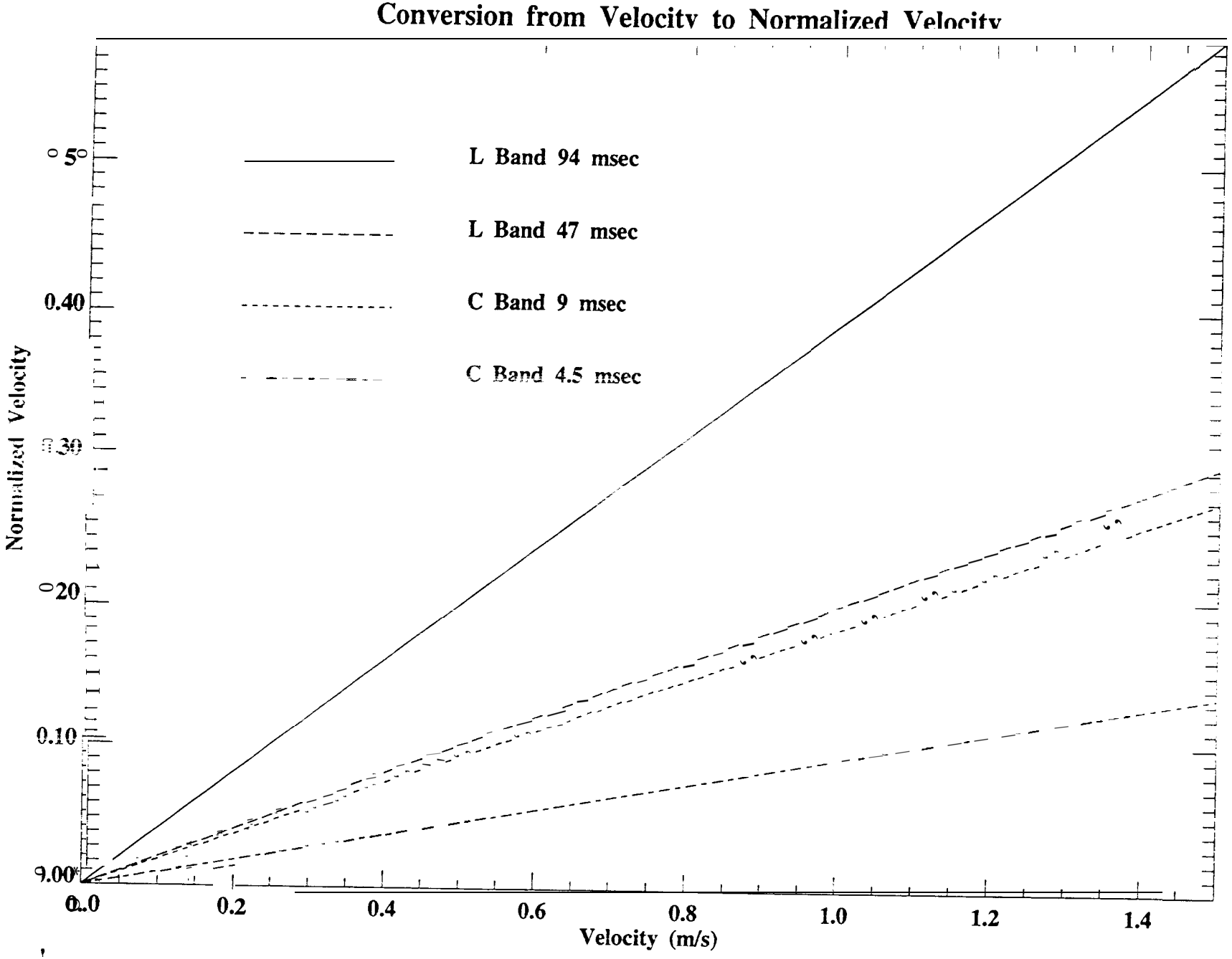
Conversion from Velocity to Normalized Velocity
L Band 94 msec
L Band 47 msec
C Band 9 msec
C Band 4.5 msec
Normalized Velocity
0.40
0.10
0.00
0.0
0.2
0.4
0.6
0.8
1.0
1.2
1.4
Velocity (m/s)

Figure 4

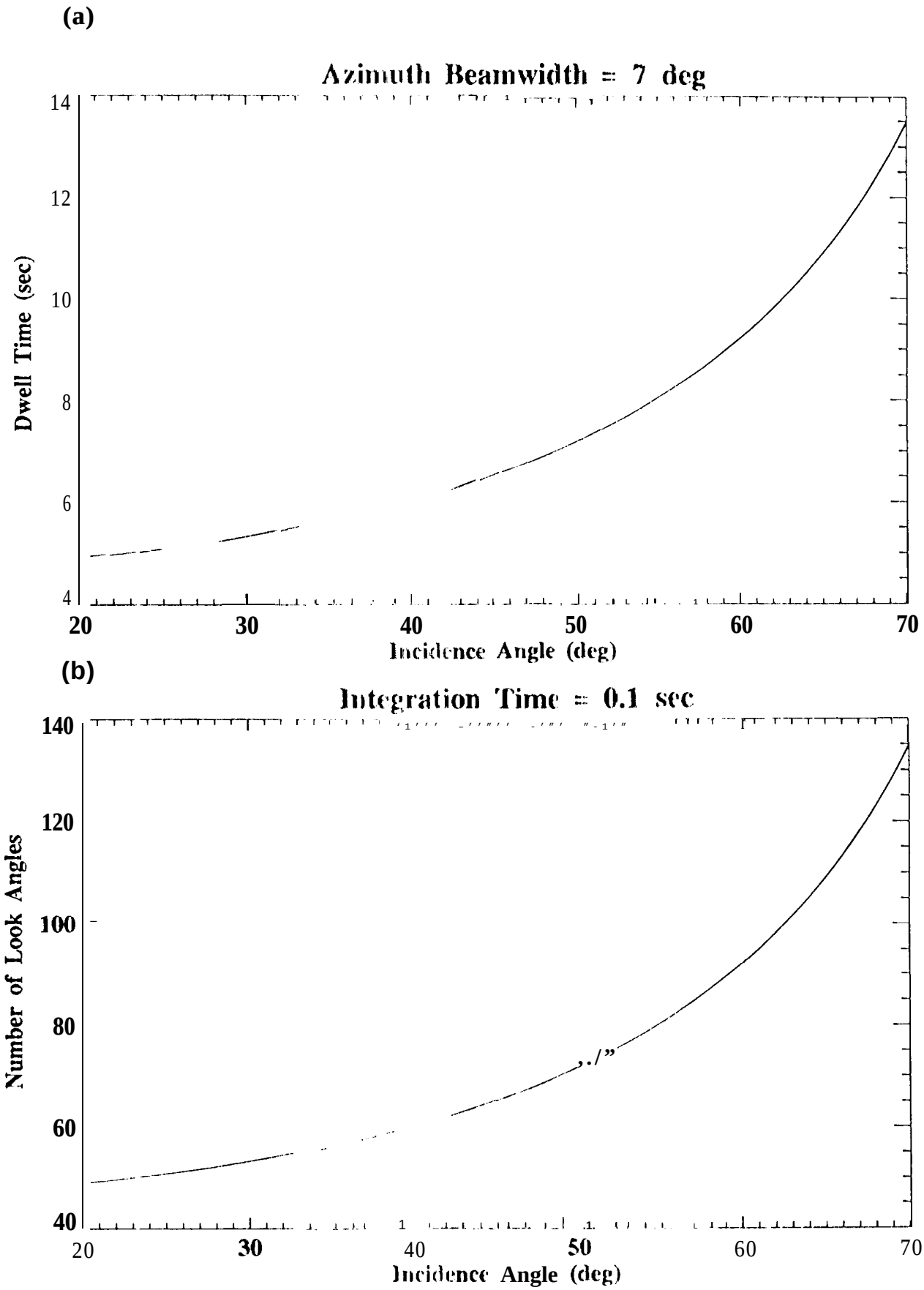
(a)
Azimuth Beamwidth = 7 deg
Dwell Time (sec)
14
12
10
8
6
4
20
30
40
50
60
70
Incidence Angle (deg)
(b)
Integration Time = 0.1 sec
Number of Look Angles
140
120
100
80
60
40
20
30
40
50
60
70
Incidence Angle (deg)

Figure 5

(a)

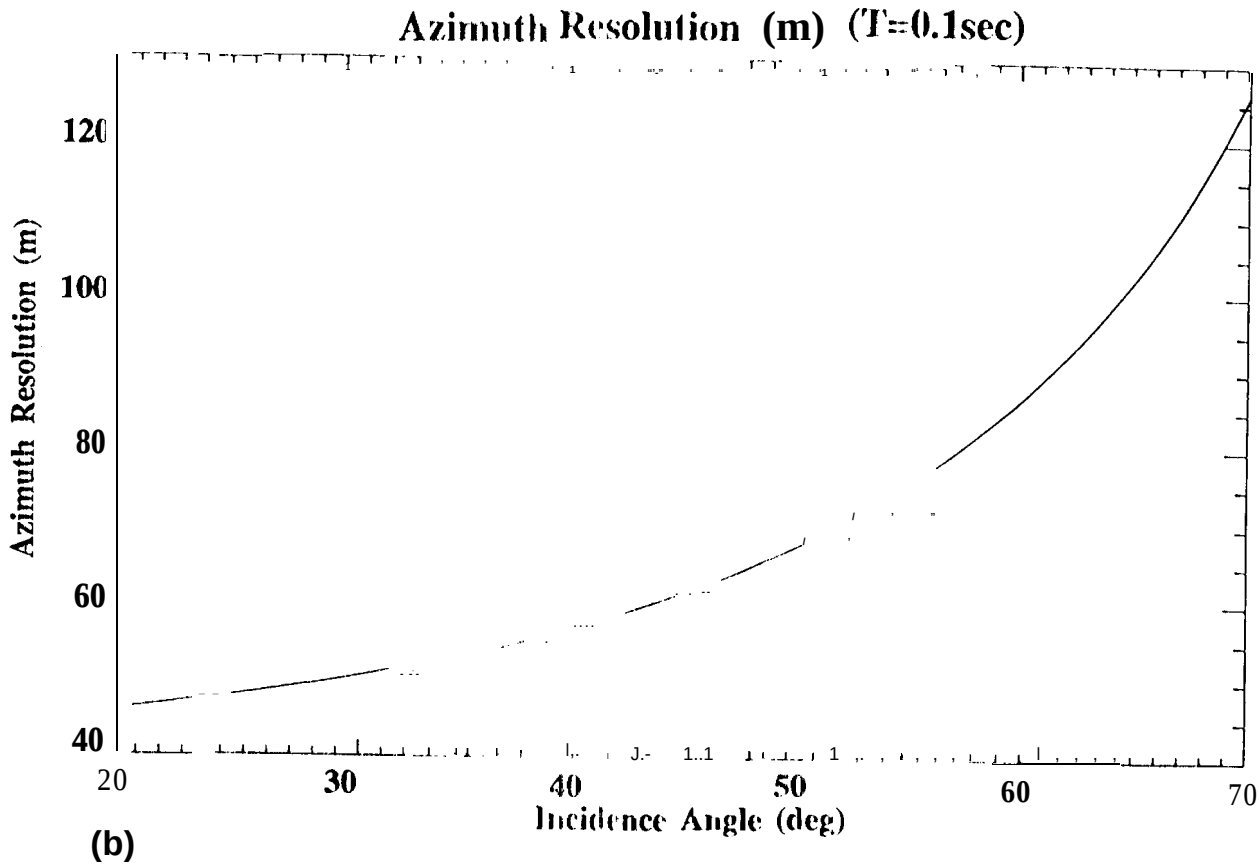
Azimuth Resolution (m) (T=0.1sec)
Azimuth Resolution (m)
120
100
80
60
40
20
30
40
50
60
70
Incidence Angle (deg)

(b)

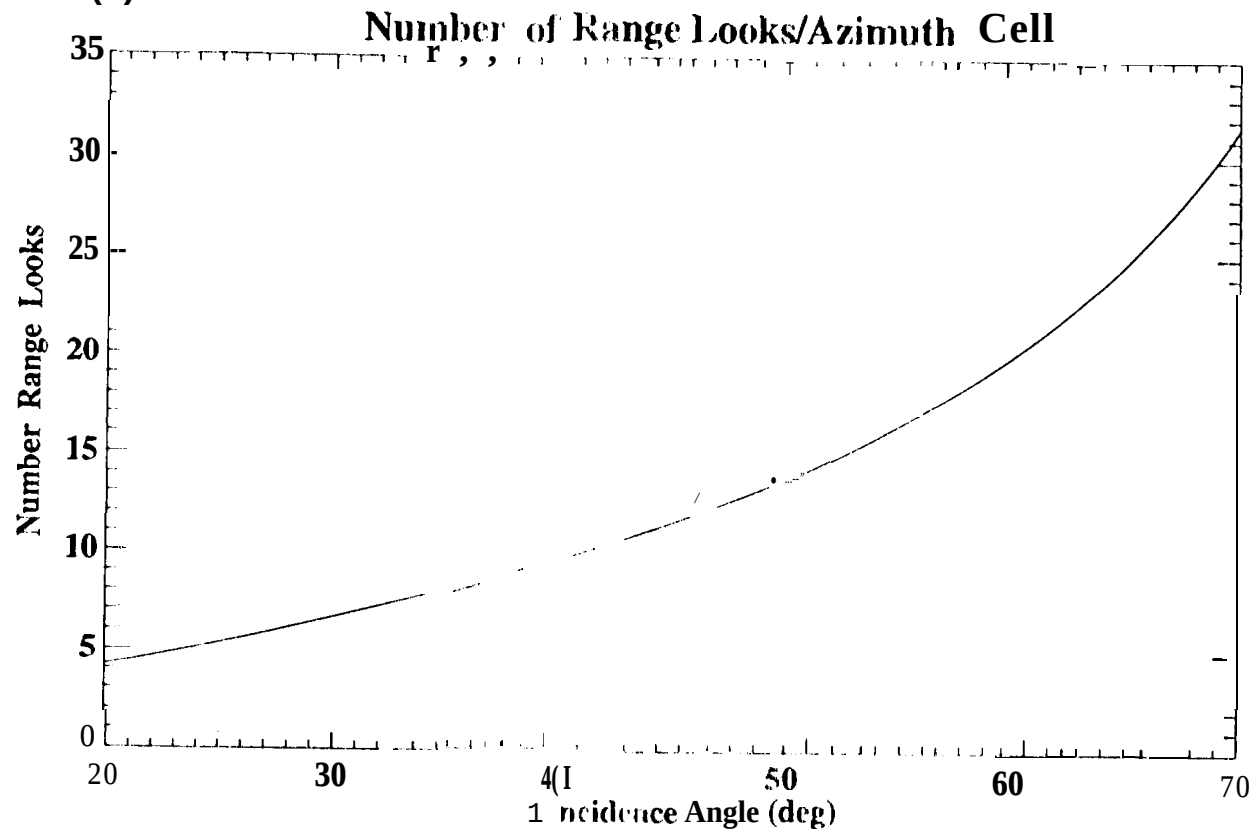
Number of Range Looks/Azimuth Cell
Number Range Looks
35
30
25
20
15
10
5
0
20
30
40
50
60
70
Incidence Angle (deg)

Figure 6

(a)

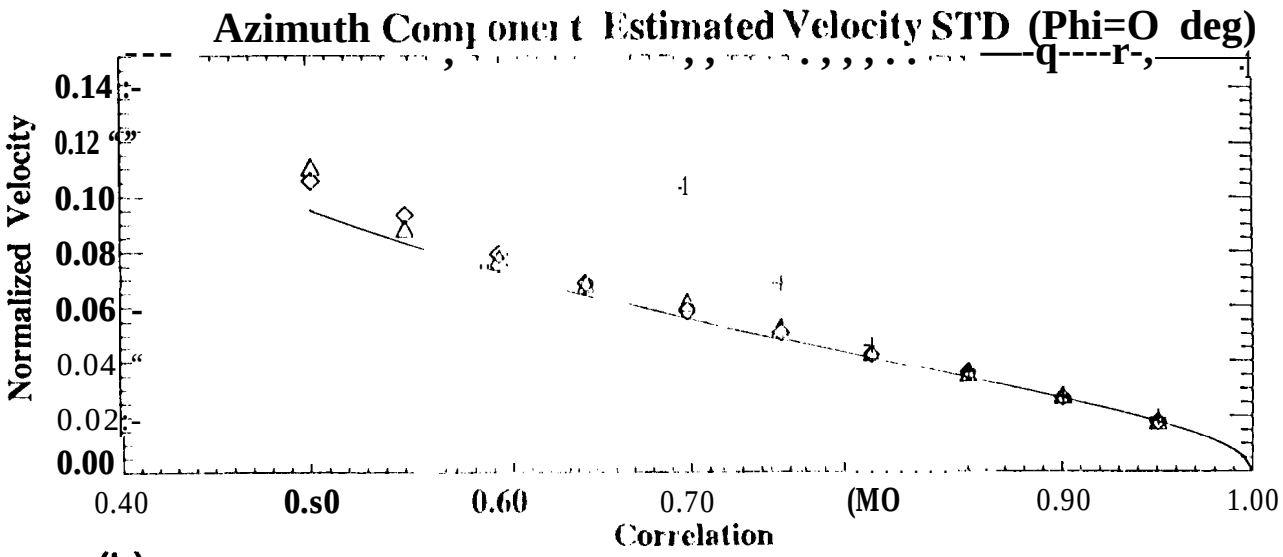
Azimuth Component Estimated Velocity STD (Phi=0 deg)
Normalized Velocity
0.14
0.12
0.10
0.08
0.06
0.04
0.02
0.00
0.40
0.50
0.60
0.70
0.80
0.90
1.00
Correlation

(b)

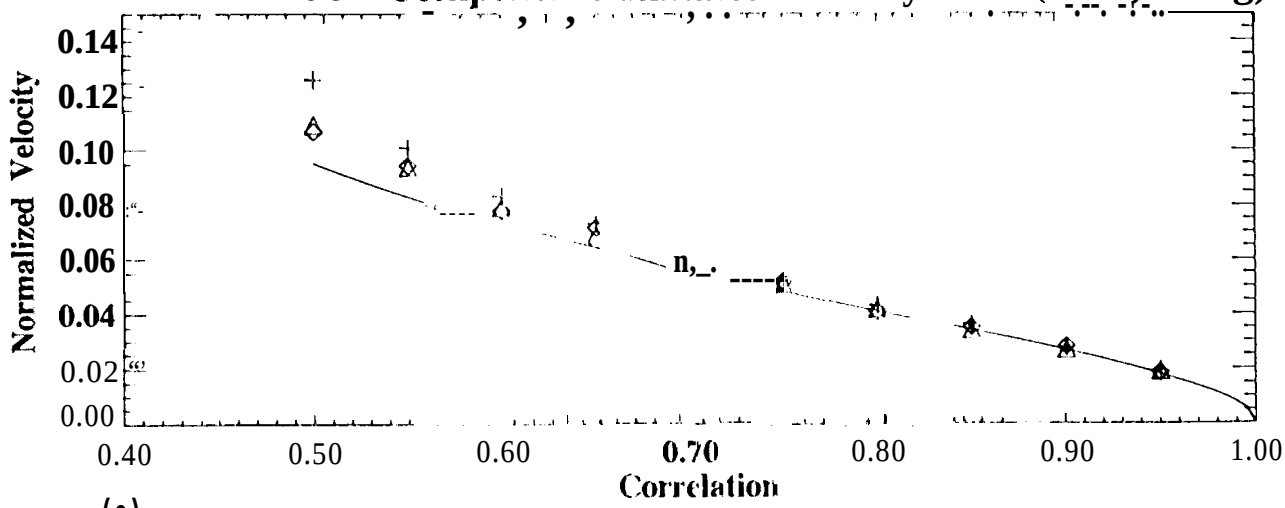
Azimuth Component Estimated Velocity STD (Phi=45 deg)
Normalized Velocity
0.14
0.12
0.10
0.08
0.06
0.04
0.02
0.00
0.40
0.50
0.60
0.70
0.80
0.90
1.00
Correlation

(c)

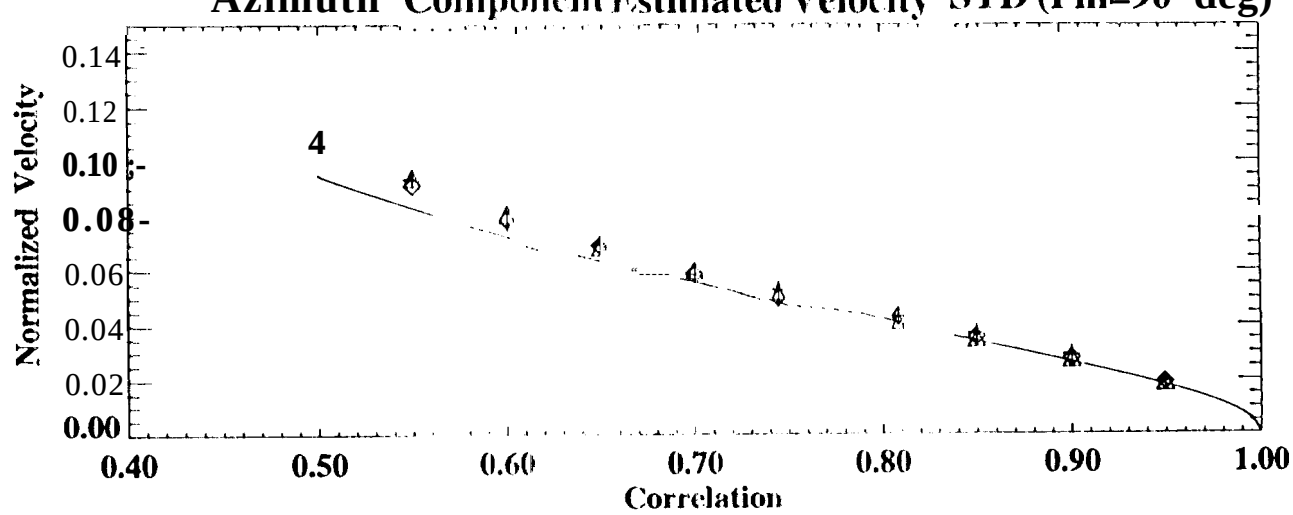
Azimuth Component Estimated Velocity STD (Phi=90 deg)
Normalized Velocity
0.14
0.12
0.10
0.08
0.06
0.04
0.02
0.00
0.40
0.50
0.60
0.70
0.80
0.90
1.00
Correlation

Figure 7

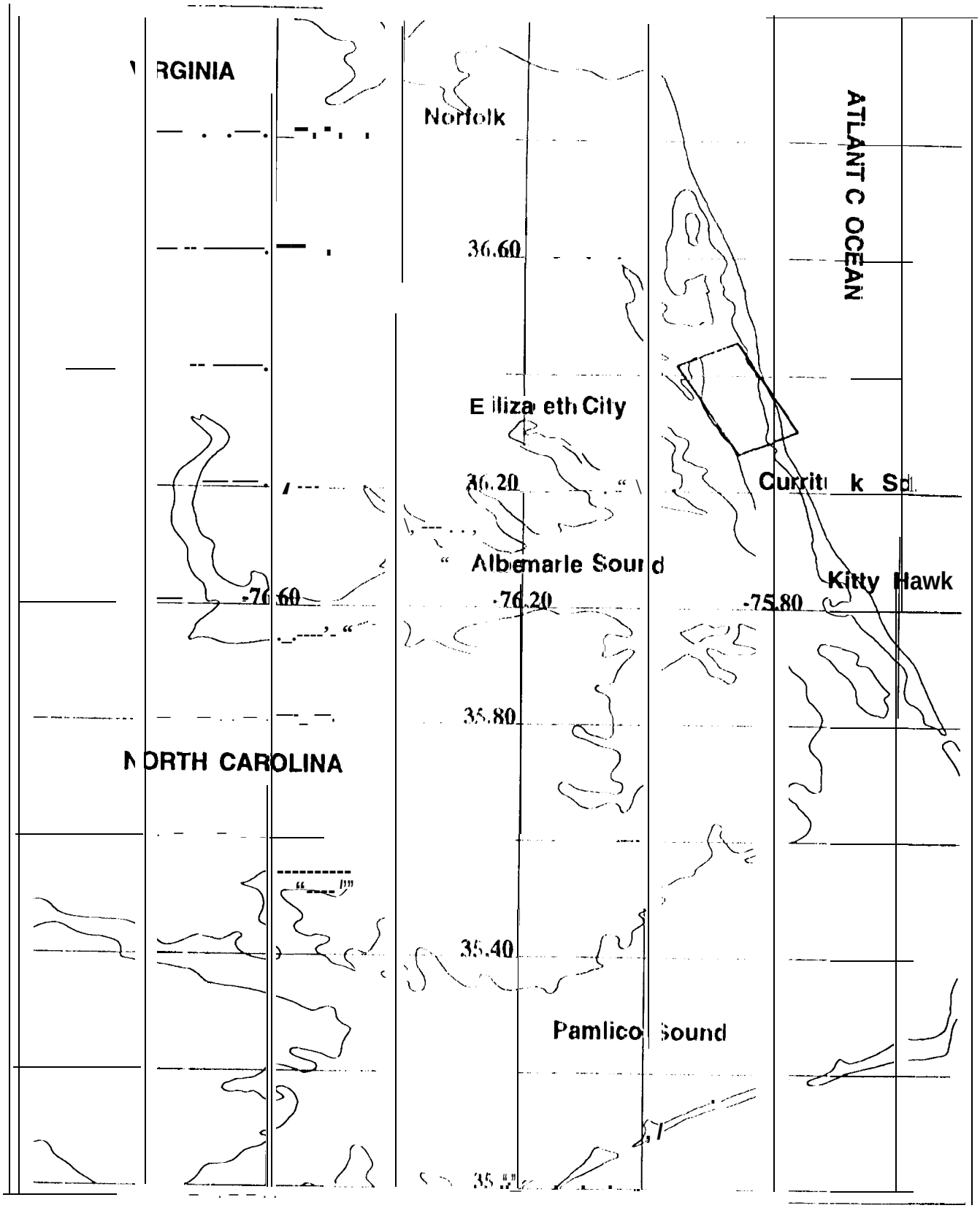
RGINIA
Norfolk
ATLANTIC OCEAN
36.60
E lizabeth City
36.20
Currituck Sd.
Albemarle Sound
Kitty Hawk
-76.60
-76.20
-75.80
35.80
NORTH CAROLINA
35.40
Pamlico Sound

Figure 8

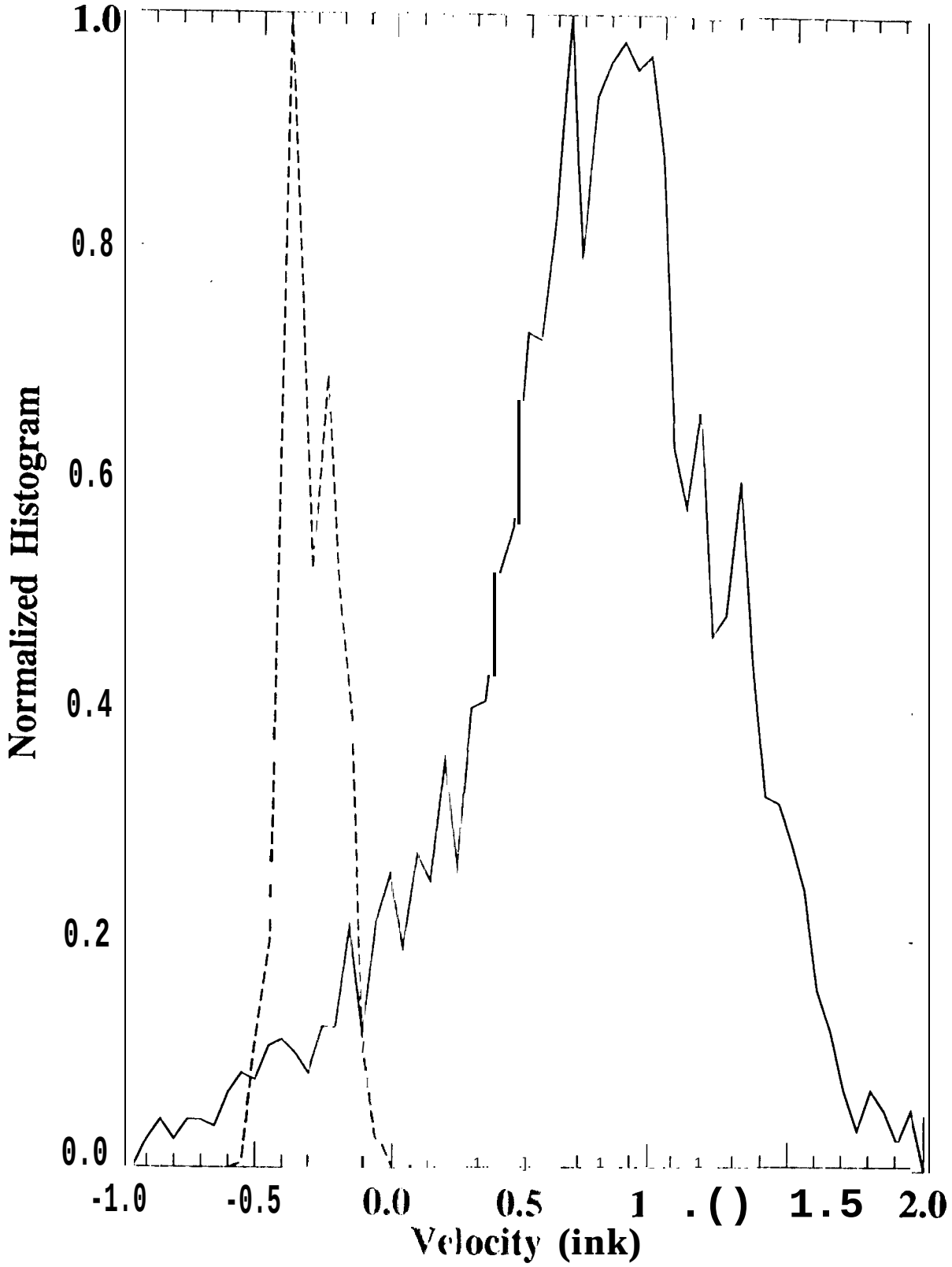
1.0
0.8
0.6
0.4
0.2
0.0
Normalized Histogram
-1.0
-0.5
0.0
0.5
1
1.5
2.0
Velocity (ink)

Figure 10

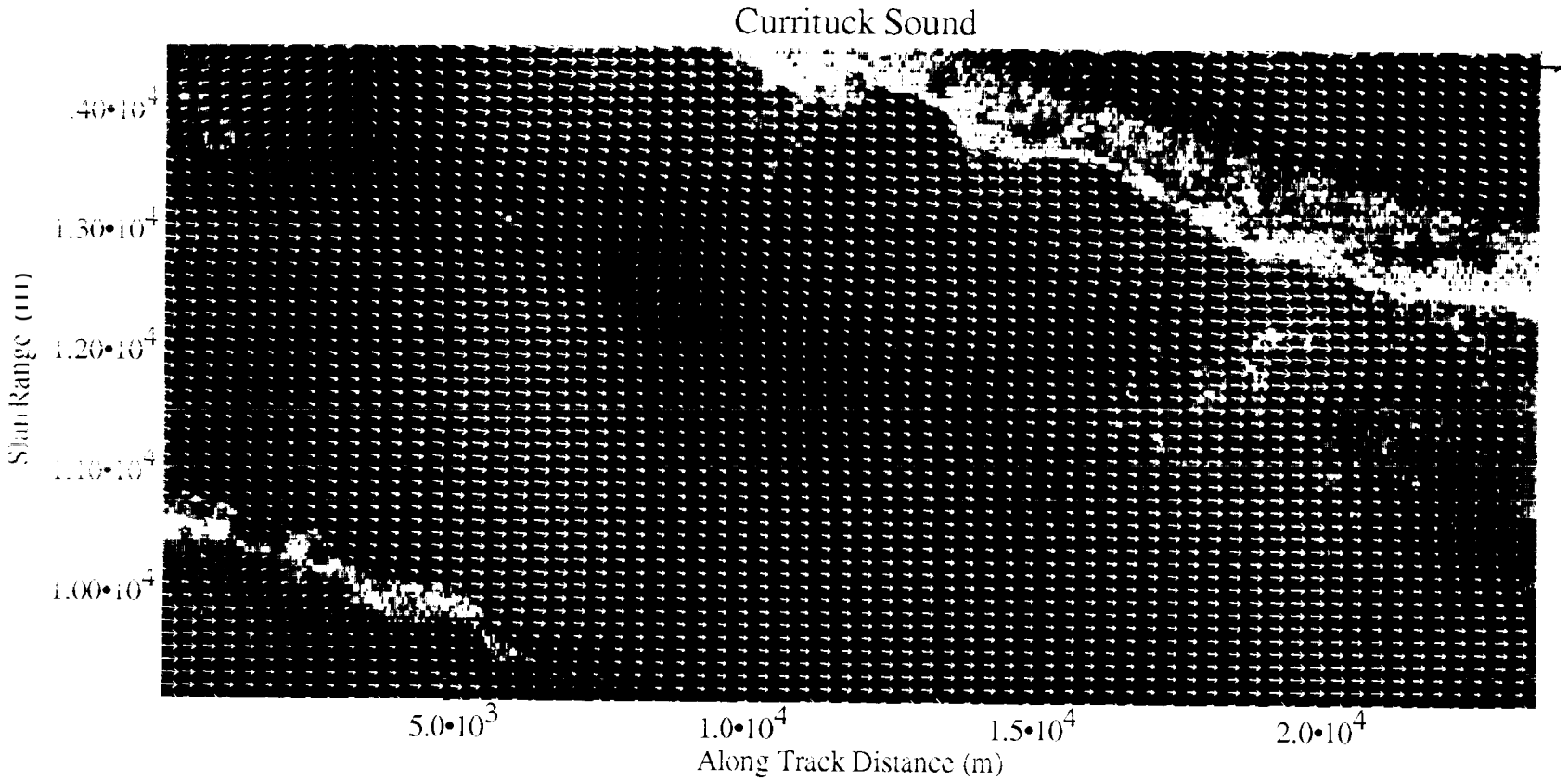
Currituck Sound
1.40•10^4
1.30•10^4
1.20•10^4
1.10•10^4
1.00•10^4
Slant Range (m)
5.0•10^3
1.0•10^4
1.5•10^4
2.0•10^4
Along Track Distance (m)